Journal of Materials Chemistry C

ROYAL SOCIETY OF CHEMISTRY

PAPER

View Article Online
View Journal | View Issue



Cite this: J. Mater. Chem. C, 2025, 13, 23259

# A self-powered and stretchable magnetic film for human–machine interface applications

Sandeep Kumar Yadav, Raksha D. Salian, Royston Mathias and Partha Kumbhakar *

Received 26th August 2025,
Accepted 12th October 2025

DOI: 10.1039/d5tc03220b

rsc.li/materials-c

Developing stretchable, self-powered electronic interfaces for ambient energy harvesting is crucial for next-generation wearable electronics and human–machine interface applications. We present a stretchable magnetoelectric composite film comprising $Ni_{0.5}Co_{0.5}Fe_2O_4$ magnetic nanoparticles embedded in an Ecoflex matrix. The nanoparticles, synthesized *via* co-precipitation, exhibit a strong magnetic response, while Ecoflex ensures high stretchability and skin-mountable adaptability. The comprehensive structural, morphological, and magnetic analyses confirm the formation of a uniform and multifunctional film. The optimized device delivers a peak output voltage of ~8.3 V and a power density of 3.16 mW $cm^{-3}$ under ambient magnetic fields, outperforming conventional soft nanogenerators. The films demonstrate excellent durability under repeated deformation and maintain stable performance at tensile strains up to ~315%. Integration into a soft wearable platform enables real-time gesture recognition, with distinct voltage signals for finger bends and gestures under low-intensity magnetic fields. This work highlights the potential of magnetic/Ecoflex-based nanogenerators in self-powered, wearable, stretchable electronics, smart prosthetics, and intelligent human–machine interfaces.



## 1. Introduction

Integrating multifunctional, flexible, and stretchable electronics into wearable technologies has accelerated the development of next-generation human–machine interfaces (HMIs), soft robotics, healthcare monitoring, smart prosthetics, and interactive electronics.[1–5] These advancements highlight the demand for skin-compatible, wearable, self-powered systems capable of real-time energy harvesting and signal detection with high mechanical adaptability.[6–9] Artificial sensory systems mimicking skin functions and responding to diverse stimuli have gained increasing attention.[10,11] A key challenge for wearable electronic devices is the absence of efficient and flexible power sources, as conventional batteries remain bulky and prone to leakage. To overcome this, researchers have advanced self-powered devices such as triboelectric nanogenerators (TENGs), piezoelectric nanogenerators (PENGs), and magnetoelectric (ME) nanogenerators. A $V_2CT_X$ MXene/silicone-based TENG has been reported with 400% stretchability and a power density of 19.75 W $m^{-2}$, enabling real-time sign-language interpretation.[12] Design strategies for wearable and implantable TENGs have also been highlighted for advancing HMI devices.[13] Polyurethane/$BaTiO_3$-based PENGs achieved 336% stretchability with an output of 31 V, successfully charging capacitors from human motion.[14] Beyond mechanical sources, ME nanogenerators based on ferromagnetic–ferroelectric core–shell nanofibers have demonstrated high AC magnetic sensitivity (760 V/T).[15] By uniquely harvesting ambient magnetic noise through strain-mediated coupling, ME devices enable wireless power supply and magnetic sensing, making them promising for IoT systems and skin-conformable wearables.[16–19]

HMI systems enable intuitive interactions between humans and machines, soft robotics, advancing wearables, and healthcare. They provide flexibility, real-time feedback, and energy efficiency, with soft sensors standing out for their adaptability, stretchability, and skin-like responsiveness. These sensors operate through various transduction principles, including capacitive mechanisms (*e.g.*, organo-hydrogel films[20] and Au-PDMS flexible films[21]), piezoelectric mechanisms (*e.g.*, ZnO-PVDF composite films[22] and ZnO-PDMS stretchable films[23]), and triboelectric mechanisms (*e.g.*, flexible PTFE films[24] and nitrocellulose membrane films[25]). TENGs and PENGs enable energy harvesting but rely on continuous deformation, limiting wearable stability. In contrast, ME nanogenerators harvest ambient magnetic noise without deformation, offering wireless and self-powered operation. They are promising for health-monitoring patches, biosensors, and smart textiles, though their use in HMIs is still limited.[26,27] Conventional ceramic-based ME composites are rigid, while emerging polymer-based systems provide stretchable, lightweight, and skin-conformable alternatives for next-generation wearable HMIs.

To address these challenges, we fabricated a stretchable ME nanogenerator film by embedding $Ni_{0.5}Co_{0.5}Fe_2O_4$

*Department of Physics and Electronics, Christ University, Bangalore, 560029, India. E-mail: partha.kumbhakar@christuniversity.in*

nanoparticles in an Ecoflex matrix. The spinel ferrite $Ni_{0.5}Co_{0.5}Fe_2O_4$ exhibits an excellent magnetostrictive response, chemical stability, and high resistivity.[28] Ecoflex, a silicone-based elastomer, offers an ultralow modulus, high strain, and biocompatibility and is widely used in soft robotics and wearable sensors for its flexibility and moisture resistance.[29] Unlike hydrogels or liquid metals, Ecoflex withstands large strain cycles while maintaining viscoelastic and dielectric stability, making it an ideal host for rigid fillers. However, ME composites based on Ecoflex remain underexplored. The resulting $Ni_{0.5}Co_{0.5}Fe_2O_4$/Ecoflex film combines elasticity and durability with efficient low-frequency magnetic energy harvesting, a resource largely untapped by TENGs and PENGs.

In this work, we have designed a highly stretchable and self-powered ME composite film by embedding $Ni_{0.5}Co_{0.5}Fe_2O_4$ nanoparticles into a soft Ecoflex matrix for skin-compatible magnetic field sensors, self-powered HMIs, and energy harvesting in wearable healthcare. Combining ferrite's magnetic properties with Ecoflex's stretchability and biocompatibility ensures stable, deformation-free operation under bending or stretching. With optimized power density, these films enable real-time applications such as self-powered biosensors, smart patches, and gesture-based interfaces for continuous health monitoring.

## 2. Experimental section

### 2.1. Materials used

Nickel nitrate hexahydrate [$Ni(NO_3)_2{\cdot}6H_2O$, Sigma-Aldrich, India], cobalt nitrate hexahydrate [$Co(NO_3)_2{\cdot}6H_2O$, Sigma-Aldrich, India], iron nitrate nonahydrate [$Fe(NO_3)_3{\cdot}9H_2O$, Sigma-Aldrich, India], and sodium hydroxide pellets [NaOH, Loba Chemie, India] were used as the initial materials. Also, Ecoflex™ was obtained from Smooth-On Inc., USA. All chemicals were used as received without additional purification. Deionized (DI) water, sourced from double-distilled water, was used as the solvent for precursor salts during the synthesis of $Ni_{0.5}Co_{0.5}Fe_2O_4$ nanoparticles.

### 2.2. Synthesis of $Ni_{0.5}Co_{0.5}Fe_2O_4$ nanoparticles and the Ecoflex film and device fabrication

$Ni_{0.5}Co_{0.5}Fe_2O_4$ nanoparticles were prepared *via* co-precipitation following the reported literature.[30] Stoichiometric amounts of $Ni(NO_3)_2{\cdot}6H_2O$, $Co(NO_3)_2{\cdot}6H_2O$, and $Fe(NO_3)_3{\cdot}9H_2O$ were dissolved in 20 mL of DI water, then combined and stirred magnetically at room temperature for 8 h at 400 rpm using a magnetic stirrer (REMI-1MLH, India). The solution mixture was kept under magnetic stirring to obtain a homogeneous solution. Then, the mixture was heated to 85 °C, and 1 M NaOH was added dropwise to achieve a pH of 12. A dark brown precipitate formed, which was further stirred at 85 °C for 6 hours until the completion of the reaction. This precipitate was separated by centrifugation, washed twice with DI water and ethanol, and dried in an oven at 200 °C for 10 h. The centrifugation was carried out at 10000 rpm for 10 minutes for each washing medium. We used a centrifuge machine (MICROSIL, India) for this process. The precipitate was washed with DI water and acetone for the first two times. Thereafter, ethanol was utilized twice for washing. Then the precipitate was collected and dried further. The resulting nanoparticles were then subjected to further characterization and analysis. To prepare the Ecoflex solution, Ecoflex™ 00-50's part A and part B were combined in a 1 : 1 ratio in 20 mL plastic vials. For the Ecoflex™–$Ni_{0.5}Co_{0.5}Fe_2O_4$ composite films, $Ni_{0.5}Co_{0.5}Fe_2O_4$ nanoparticles were incorporated into the Ecoflex solution at 0.6 wt% and 2 wt% in a glass beaker by simple manual mixing with a wooden spatula until uniform distribution was achieved. The mixtures were then drop-cast onto Petri dishes and dried at RT for 24 h. The resulting flexible and stretchable films (NC1 and NC2) were carefully peeled from the Petri dishes and used for further characterization. The steps involved in film preparation are shown in Fig. S1 (SI). The dimensions of both films were maintained with a tolerance of 2.5 ($\pm$ 0.1) × 1 ($\pm$ 0.05) cm × 0.1 ($\pm$ 0.01) cm. For the analysis and demonstration of energy harvesting and real-time applications, copper electrodes were attached to both sides of the top and bottom surfaces of the films. Fig. 1(a) illustrates magnetic field harvesting and HMI application using a stretchable magnetic Ecoflex film. Furthermore, the device was fabricated in a horizontal configuration with copper electrodes attached to the top and bottom surfaces of the film due to its glue and easy stickiness, enabling stable contact and reliable output measurement, and a complete set of copper electrode films are shown in Fig. S2 (SI).

### 2.3. Characterization techniques

The phase formation of the synthesized spinel ferrite $Ni_{0.5}Co_{0.5}Fe_2O_4$ was confirmed through X-ray diffraction (XRD) analysis using a diffractometer (Bruker D8 Advance) equipped with Cu-K$\alpha$ radiation ($\lambda$ = 1.540 Å). Fourier-transform infrared (FTIR) spectroscopy was carried out using a NEXUS 870 instrument, covering the spectral range of 400–4000 $cm^{-1}$. Surface morphology was examined using a field-emission scanning electron microscope (FE-SEM, Thermo Fisher Apreo) and an analytical transmission electron microscope (analytical TEM). To assess the device performance, a custom-designed Helmholtz coil was fabricated using 3D printing technology (Pratham, Make3D.in). Each coil's base was 3D-printed using the PLA material with a diameter of 8 cm. A 0.5-mm-thick enameled copper wire was wound 25 times around each base to form a pair of identical coils. The enamel coating at the wire ends was stripped to ensure proper electrical connectivity. To achieve the maximum magnetic field at the center, the coils were positioned 4 cm apart. Both coils were connected in parallel to a variable 2.2 A current source, with the polarity configured to ensure the current in each coil flowed in the same direction, producing a magnetic field of 1.33 mT. Further details on the schematic experimental setup and the fabrication of the Helmholtz coil are given in Fig. S3(a)–(c) (SI). Strain–stress analysis of the films was carried out using a universal tensile testing machine (UTTM). The electrical response of the ME devices was measured using a digital oscilloscope (Tektronix, TBS 1000C series), allowing precise output voltage evaluation.

 

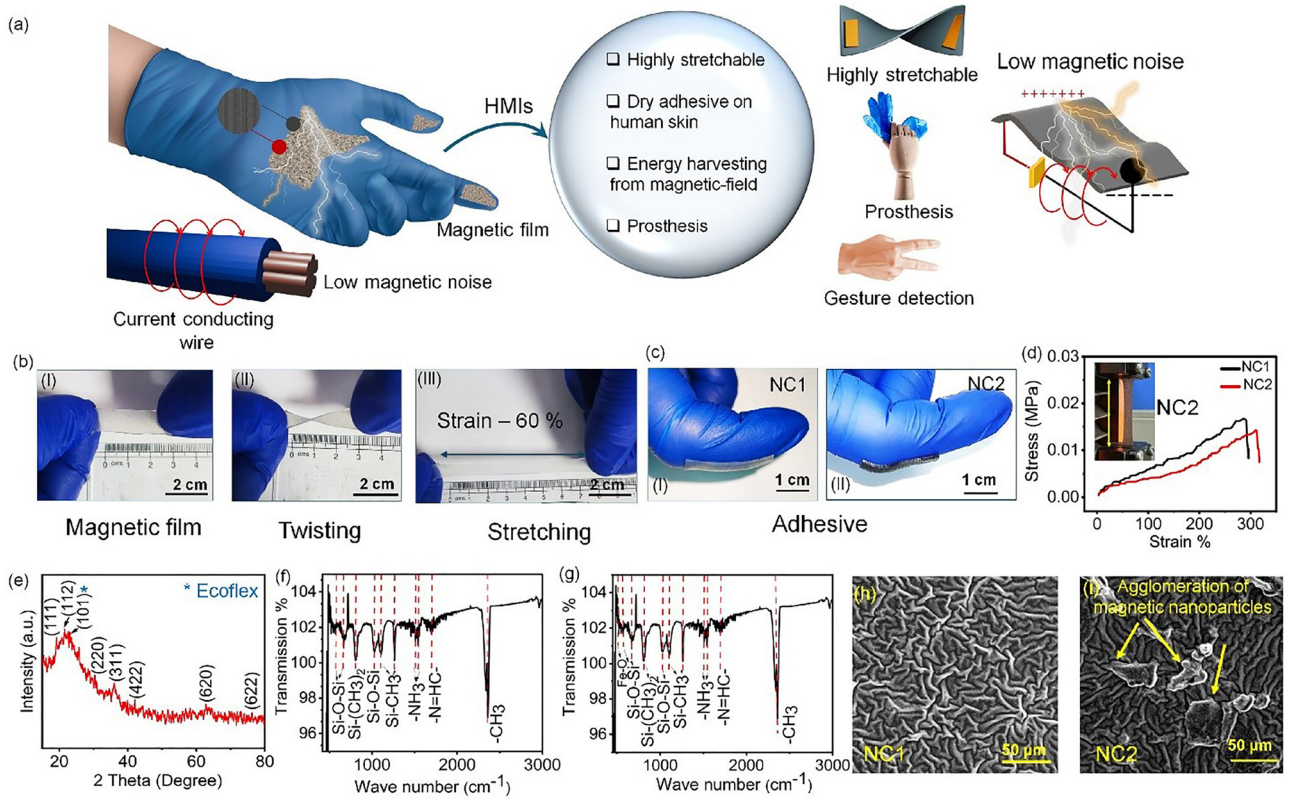


Fig. 1 (a) Magnetic field harvesting, an HMI application using a wearable and stretchable magnetic Ecoflex film. Digital images of the (b) flat, twisted, and stretched orientations of NC1 films, (c) adhesiveness of NC1 and NC2 on the glove, (d) stress–strain graph of NC1 and NC2 films (inset: digital image of the NC2 film with the UTTM setup), (e) XRD pattern of the NC1 film, (f) FTIR spectrum of the NC1 film, and (g) FTIR spectrum of the NC2 film. FESEM images of (h) NC1 and (i) NC2 films.

## 3. Results and discussion

### 3.1. Structural, functional, and morphological analyses

The digital images of NC1 films in flat, twisted, and stretched orientations are shown in Fig. 1(b)(I), (b)(II), and (b)(III), respectively, demonstrating their mechanical flexibility. The digital image of the NC1 and NC2 films illustrating its adhesion to the glove is shown in Fig. 1(c). Similarly, the flat, twisting, and stretchable characteristics of the NC2 film are shown in Fig. S4(a) of the SI. For mechanical strength testing, both films with similar dimensions (25 mm × 10 mm × 1 mm) were mounted on a universal tensile testing machine, with a constant elongation rate of 5 mm per minute to ensure uniform deformation. The NC1 film exhibited a progressive increase in strain with applied stress, achieving a maximum elongation of ~291% of its original length before fracture, which occurred at ~295% beyond its peak elongation. The corresponding load at failure was 0.15 kgF, and the peak tensile strength was calculated as 0.167 MPa. In comparison, the NC2 film demonstrated a maximum elongation of ~311% and failed at ~317% elongation, with a breakdown load of 0.13 kgF and a peak tensile strength of 0.142 MPa. The stress–strain profiles of the NC1 and NC2 composite transducer films are shown in Fig. 1(d). The inset of Fig. 1(d) shows the digital image of the NC2 film during mechanical strength measurements. Similarly, the digital image of straightness measurement for NC1 is shown in Fig. S4(b) (SI). Also, the Young's moduli of NC1 and NC2 are $4.9 \times 10^{-5}$ MPa and $3.9 \times 10^{-5}$ MPa, respectively. Furthermore, during the experimental procedures, both films were analyzed under strains of up to only 60%. These findings highlight the mechanical robustness and high strain tolerance of NC1 and NC2 films, underscoring their potential for use in flexible and stretchable electronic applications. The diffraction peaks of the embedded $Ni_{0.5}Co_{0.5}Fe_2O_4$ magnetic nanoparticles match the standard JCPDS cards (No. 74-2081) and (No. 22-1086) for $NiFe_2O_4$ and $CoFe_2O_4$, respectively, confirming the successful formation of a pure $Ni_{0.5}Co_{0.5}Fe_2O_4$ ferrite phase[30] with a cubic crystal structure as shown in Fig. S4(c). Furthermore, Fig. 1(e) presents the XRD pattern of the NC1 films and a broad peak is observed at 22.4°, corresponding to the (101) plane of the Ecoflex matrix, consistent with the amorphous nature of silicone-based elastomers.[29] Also, the XRD pattern of the NC2 film is shown in Fig. S4(d) to distinguish the peaks of Ecoflex in the compositions. The HR-TEM image of $Ni_{0.5}Co_{0.5}Fe_2O_4$ nanoparticles is provided in the SI (Fig. S4(e)). The HR-TEM analysis revealed the crystalline nature of $Ni_{0.5}Co_{0.5}Fe_2O_4$ nanoparticles. The magnetic measurement of $Ni_{0.5}Co_{0.5}Fe_2O_4$ is shown in Fig. S4(f), and the nanoparticles are found to have ferromagnetic nature. FTIR spectroscopy of NC1 and NC2 was further conducted to verify the composite's chemical structure and bonding characteristics,

as shown in Fig. 1(f) and (g). The NC1 and NC2 films display characteristic stretching bands around 480 and 490 $cm^{-1}$, which are attributed to Fe–O stretching vibrations within the $Ni_{0.5}Co_{0.5}Fe_2O_4$ phase. Additional prominent peaks at 574, 654, 804, and 1015 $cm^{-1}$ correspond to the Si–O–Si stretching vibrations, indicative of the siloxane characteristic of Ecoflex.[29] Peaks at 1257 and 787 $cm^{-1}$ are assigned to Si–C stretching in $Si–CH_3$ and $Si–(CH_3)_2$ groups, respectively. Furthermore, the bands at 1509 and 1548 $cm^{-1}$ are associated with the symmetric and asymmetric bending vibrations of $–NH_3$ groups, while a notable peak at 1704 $cm^{-1}$ corresponds to the stretching vibration of imine groups (–HC═N–) in the film. A distinct absorption band at 2367 $cm^{-1}$ is attributed to C–H stretching in the methyl groups of the Ecoflex matrix.[31] The FE-SEM images of NC1 and NC2 films are shown in Fig. 1(h) and 1(i), respectively. From the FESEM analysis, NC1 and NC2 films contain magnetic nanoparticles uniformly embedded in the Ecoflex matrix. In the FESEM image of NC1, the nanoparticles are well dispersed within the bulk matrix and are not prominently visible on the surface, as shown in Fig. 1(h). In contrast, the NC2 film contains a higher wt% of magnetic nanoparticles, and some of these particles or their agglomerates are exposed at the surface, which appear as brighter features in the FESEM image, as shown in Fig. 1(i). The surface morphology impels the film's adherence to human skin, which displays a textured structure reminiscent of human skin. The synthetic skin-like surface morphology enhances conformal contact with soft and irregular surfaces, such as human skin, by mimicking its flexible, stretchable, and adaptive properties, ensuring stable operation of wearable HMI devices during body movements. This morphology improves adhesion to the body's contours and maintains consistent contact for reliable sensor or electrode function.[29]

### 3.2. Wireless power transmission analysis

A ME nanogenerator, utilizing nanoparticle–Ecoflex composites, was experimentally designed to efficiently harvest energy from low-intensity ambient magnetic fields, as illustrated in Fig. 2(a). A Helmholtz coil generated an alternating magnetic field of 1.33 mT at 50 Hz, and a DSO was utilized for the measurement of the device's output voltage, as shown in Fig. 2(b) and Fig. S3. The reorientation of magnetic domains causes magnetostrictive deformation of the spinel-structured $Ni_{0.5}Co_{0.5}Fe_2O_4$ nanoparticles when exposed to an external magnetic field. An alternating voltage signal is produced when this dynamic strain is transmitted to the interface *via* the elastic Ecoflex matrix, causing an electrical response.[32] Here, we have measured the peak-to-peak voltage ($V_{pp}$) for the NC1 devices in three deformation states such as flat (Fig. 2(c)), twisted

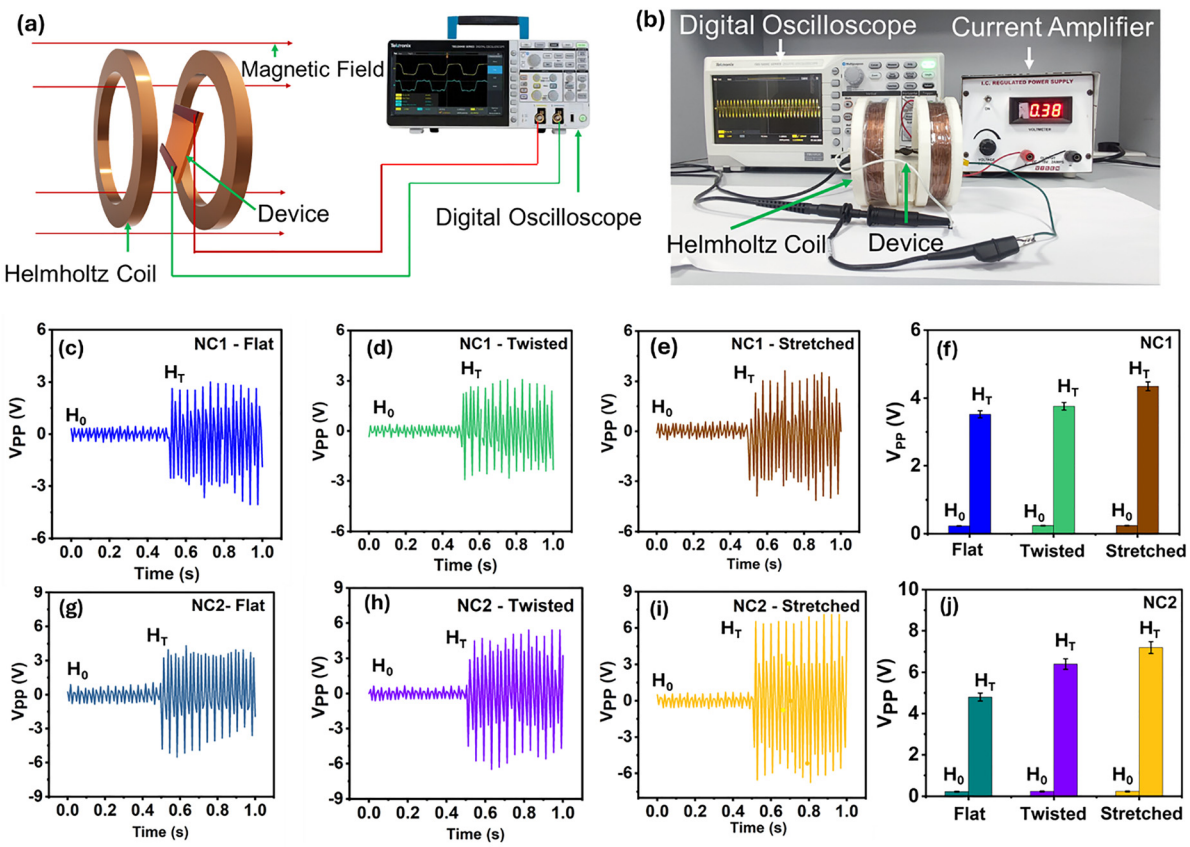


Fig. 2 (a) Schematic diagram of the low-intensity magnetic field harvesting experimental setup. (b) Digital image of the experimental setup. (c)–(e) Output $V_{pp}$ from the NC1 device in flat, twisted, and stretched orientations. (f) Output $V_{pp}$ from the NC1 device at $H_0$ and $H_T$ (trial number, $n$ = 10). (g)–(i) Output $V_{pp}$ from the NC2 device in flat, twisted, and stretched orientations. (j) Output $V_{pp}$ from the NC2 device at $H_0$ and $H_T$.

 

(Fig. 2(d)), and stretched (Fig. 2(e)) in the absence ($H_0$ = 0 T) and presence ($H_T$ = 1.33 mT) of magnetic fields. The corresponding output voltage with error bars, are presented for comparison in the bar diagram in Fig. 2(f). Similar procedures were performed for the NC2 device, and the results are shown in Fig. 2(g)–(j). Each experimental result was obtained through multiple measurements. To evaluate the stability of the output voltage from the wearable HMI device, measurements were conducted repeatedly ($n$ = 10), and the results are presented in Fig. 2(f) and (j), with error bars representing the standard deviation to indicate measurement consistency and reliability. The output voltage was recorded across 10 trials, with each data point reflecting the mean value of the recorded voltages. This statistical approach ensures a robust assessment of the device's performance, thereby confirming the device's stability and reproducibility under dynamic conditions. These results show that changing the device's shape (stretching and twisting) strengthens its electrical response with a constant magnetic field. The comparison analysis showed that NC2 outperformed NC1, likely due to its higher magnetic nanoparticle density, which increases strain and transduction efficiency. Higher nanoparticle content enhances magnetic dipole interactions with the Ecoflex matrix, amplifying the magnetostrictive effect and enabling more effective conversion of magnetic stimuli into electrical signals in NC2 for wearable HMI devices.

While keeping the magnetic excitation constant, the device's performance was assessed in various mechanical deformation states, including flat, twisted, and stretched (demonstrating stable operation at ~60% strain) conditions. These setups mimic mechanical challenges pertinent to stretchable and wearable HMI systems. Consistent with previous research on stretchable ME composites, improved strain transfer, optimized magnetic domain alignment, and enhanced interfacial coupling between the magnetostrictive filler and the elastomeric host have been associated with the increased voltage output under deformation.[33,34] $Ni_{0.5}Co_{0.5}Fe_2O_4$ was selected due to its significantly higher piezomagnetic constant $\left(\frac{\partial\lambda}{\partial H} = 1.74 \times 10^{-9}\ A^{-1}\ m\right)$ than other compositions, as reported in the literature,[32] resulting in superior piezomagnetic performance. In spinel ferrites ($AB_2O_4$), the magnetic moments of ions in tetrahedral (A) and octahedral (B) sites are oriented antiparallel to each other. In $NiFe_2O_4$, the spins of $Fe^{3+}$ ions at A and B sites are antiparallel and largely cancel each other, yielding a net magnetic moment of ~$2\mu_B$ due to the presence of $Ni^{2+}$ ($2\mu_B$, two unpaired electrons) at B sites. Substituting $Co^{2+}$ ($3\mu_B$, two unpaired electrons) preferentially into B sites replaces $Ni^{2+}$ and increases the number of unpaired electrons at octahedral sites, which enhances the magnetic properties. Furthermore, $Co^{2+}$ exhibits higher magnetic anisotropy than $Ni^{2+}$, resulting in an increased coercivity ($H_c$) with Co substitution. This arises from the higher anisotropy field associated with $Co^{2+}$, which increases the domain wall energy and thus contributes to a more substantial piezomagnetic effect.[33,35,36] This mixed-metal composition allows for the adjustment of magnetic sensitivity, making it work more effectively than

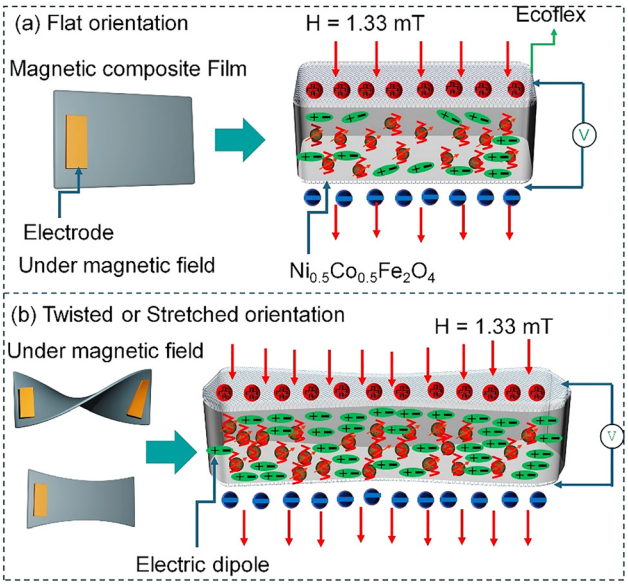


Fig. 3 Illustration of magnetic–electric dipole interactions in ME films in (a) flat and (b) twisted or stretched orientations.

single-metal ferrites. It is observed that the twisted or stretched conditions of the NC1 and NC2 nanogenerators yield higher output voltages compared to the conditions without strain. This phenomenon can be explained as follows: when the magnetic nanoparticle-embedded Ecoflex film is flat, a limited number of electric dipoles inside the matrix are aligned, resulting in a weak magnetic–electric interaction, and this limited coupling leads to lower voltage generation, as shown schematically in Fig. 3(a). However, mechanical stress redistributes through the Ecoflex matrix when the film twists or stretches, encouraging more electric dipoles to align effectively and enhancing the dipole.[37,38] This enhanced dipole alignment increases the interfacial interactions between the dipoles in the matrix and embedded magnetic nanoparticles, resulting in a stronger ME coupling, as shown in the schematic in Fig. 3(b). Consequently, the film's voltage generation is significantly enhanced, which can be rationalized through mathematical formulation. The general expression can be represented by the ME voltage coefficient ($\alpha_V^H$).[39–41] The ME voltage coefficient establishes a direct correlation between the induced electric field ($E$) and the externally applied magnetic field ($H$), expressed as $\alpha_V^H = \frac{\partial V}{\partial H}$. A higher $\alpha_V^H$ value indicates stronger magnetoelectric coupling, explaining the increased output voltage generation. Such dependence highlights the fundamental role of interfacial strain transfer and dipole alignment in boosting the ME response. The detailed derivation of this formulation, including the role of interfacial strain transfer, is provided in the SI.

Furthermore, the ME nanogenerator was connected with a rectification system capable of harvesting, converting, and storing the generated electrical energy in storage elements such as capacitors or batteries, as shown in Fig. 4(a). The system was systematically tested across various external load resistances

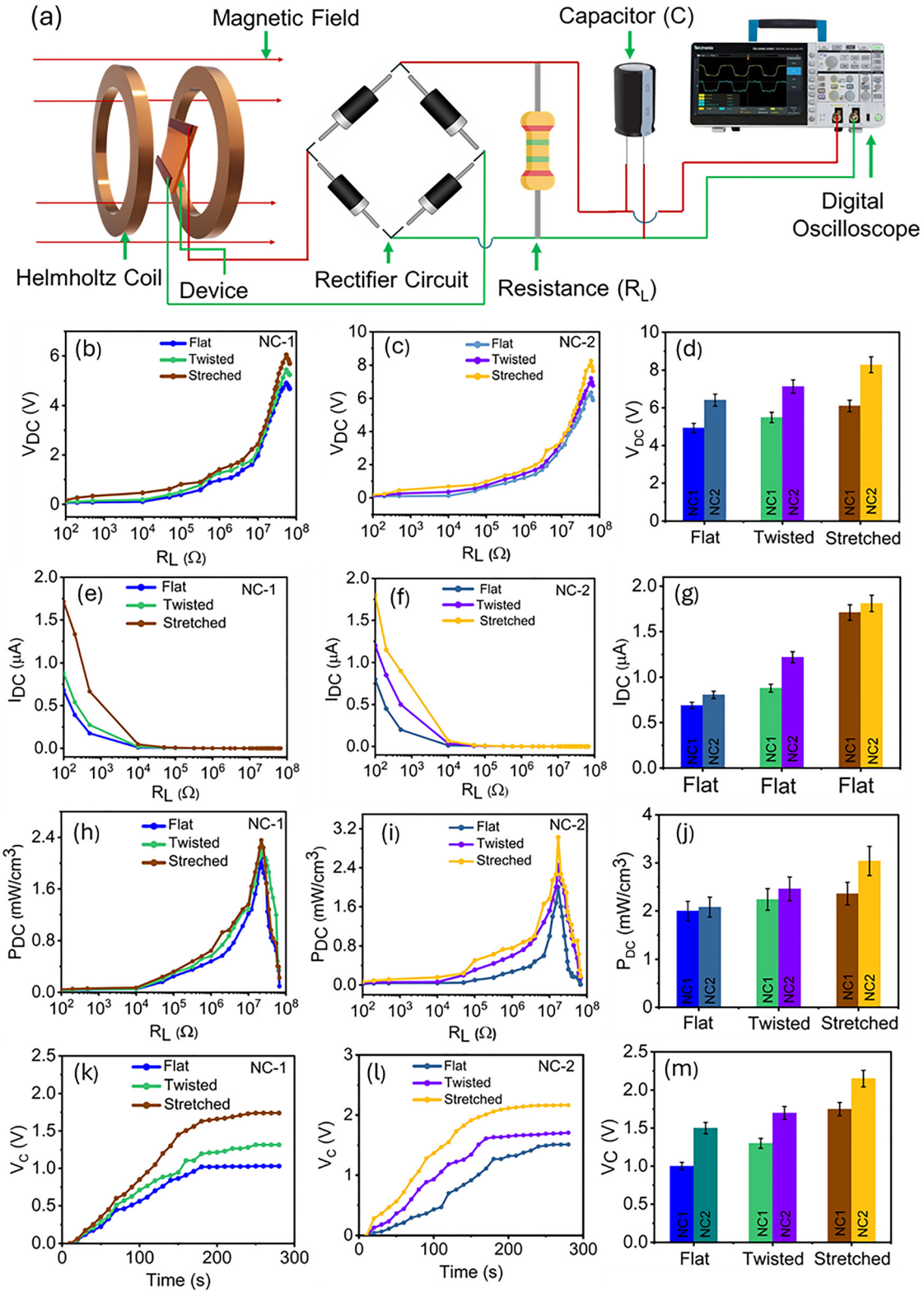


Fig. 4 (a) Schematic of the simplified circuit diagram with a ME transducer, a full-bridge rectifier, a capacitor, and a load resistance. $V_{DC}$ under varying loads for (b) NC1 and (c) NC2 devices. (d) Bar chart comparing the $V_{DC}$ of NC1 and NC2. $I_{DC}$ output from (e) NC1 and (f) NC2. (g) Bar chart comparing the $I_{DC}$ of NC1 and NC2. $P_{DC}$ with load resistance for (h) NC1 and (i) NC2. (j) Bar chart comparing the $I_{DC}$ of NC1 and NC2. Charge accumulation dynamics in capacitors for (k) NC1 and (l) NC2 transducers. (m) Bar chart of the $V_C$ of NC1 and NC2.

 

($R_L \approx$ 100 Ω–100 MΩ). The DC voltage ($V_{DC}$) for the NC1 and NC2 devices is shown in Fig. 4(b) and 4(c), respectively, and summarized as a bar diagram in Fig. 4(d). The output voltage from the NC1 and NC2 devices was repeatedly recorded to ensure stability, and the results are presented in Fig. 4(d). Similar procedures were used to measure the current and power calculations. The generated DC current ($I_{DC}$) as a function of $R_L$ is plotted for both devices in Fig. 4(e) and (f). As expected, increasing load resistance led to higher DC voltage output, while $I_{DC}$ decreased accordingly, a typical behavior governed by ohmic and power transfer principles. Fig. 4(g) presents a comparative analysis of $I_{DC}$ values for NC1 and NC2 under different loading conditions. Under stretched configurations, the maximum open-circuit DC voltages were ~6.06 V for NC1 and 8.3 V for NC2. The corresponding short-circuit DC currents were measured at ~1.8 μA and ~1.7 μA, respectively. The equation used to calculate the DC power density ($P_{DC}$)[42] of the various ME transducers is as follows (eqn (1)):

$$P_{DC} = \frac{V_{DC} \times I_{DC}}{\text{Volume of the device}} \quad (1)$$

In this context, the calculated $P_{DC}$ values for NC1 and NC2 devices under varying load resistances are shown in Fig. 4(h) and 4(i), respectively. These plots display Gaussian-like distribution curves, highlighting the dependence of power output on external $R_L$. A comparative analysis of the maximum $P_{DC}$ values across different transducers is shown in Fig. 4(j). Among the two, the NC2 device, comprising a higher concentration of magnetostrictive nanoparticles, achieves a power density of ~3.16 mW cm$^{-3}$, surpassing the NC1 device, which generates ~2.36 mW cm$^{-3}$ under the same magnetic field conditions (1.33 mT at 50 Hz). Remarkably, the DC power densities obtained in this work exceed those reported in previous studies of ME energy harvesters, as shown in Fig. 4(j). For instance, a PVDF/$CoFe_2O_4$-based ME transducer generated a maximum power output of 11 μW,[43] while a PVDF/$YFeO_3$ composite-based harvester achieved a power density of 2 μW cm$^{-3}$.[44] Additionally, a polymer ink printed on a Metglas substrate yielded a power density of 0.64 mW cm$^{-3}$.[45] These findings underscore the enhanced energy harvesting capability of the NC2 ME nanogenerator, making it a promising candidate for powering next-generation wearable HMI systems. To assess the energy storage capability of our ME transducers in a capacitor, we carried out a charging process until the voltage ($V_C$) reached a saturation point over time, as illustrated in Fig. 4(k) and Fig. 4(l) for NC1 and NC2, respectively. Also, $V_C$ is summarized as shown in the bar graph in Fig. 4(m). The stored electrical energy in the capacitor was determined using eqn (2):[42]

$$E_C = \frac{1}{2} C V_C^2 \quad (2)$$

In this analysis, $C$ refers to the capacitance of the storage capacitor (100 μF), and it took approximately 5 minutes for the ME transducers to charge the capacitor to their respective saturation voltages. The NC1 and NC2 devices successfully stored maximum electrical energies of approximately 87.5 μJ and 107.5 μJ, respectively. These energy levels are sufficient to power low-energy electronic components and sensor nodes typically used in wearable and soft HMI systems, where operating power demands range from nanowatts to a few microwatts. The mechanical stretchability of the ME film was further assessed under durability testing, showing outstanding robustness as it maintained its full output performance without degradation even after 1000 continuous stretching–release cycles at 100% strain as shown in Fig. S5(a) and (b) (SI).

### 3.3. Gesture-induced voltage in ME transducer films for HMI applications

To explore the feasibility of the developed ME composite film in real-time gesture-controlled HMI systems, distinct finger bending and gestures, namely 'Victory', 'Ok', and 'Stop', were employed as representative input modalities, as shown in the schematic of Fig. 5(a). The NC1 and NC2 ME nanogenerators demonstrated enhanced electrical output performance. However, the HMI demonstrations in this study primarily highlight NC2, with the corresponding results for NC1 provided in the SI (Fig. S6). For this demonstration of gesture-based voltage generation, a power cord connected to a primary power source supplying 1 A current at 50 Hz was employed as a stray magnetic field generator, and the application was performed at a 2 cm distance from the power cord to achieve higher efficiency and output voltage recorded using a DSO. A flexible NC2 nanogenerator was connected to electrodes and subjected to index finger bending at four different angles of 0°, 5°, 65°, and 125° (Fig. 5(b)), which simulate natural finger motions during gesture input. As the bending angle increased, a corresponding increase in output voltage from ~2 V to 7 V was observed, as shown in Fig. 5(c). The clear voltage differentiation at each bending angle highlights the film's soft pressure or motion sensor capability. This energy-harvesting approach enables a self-powered system suitable for real-time motion tracking. Furthermore, for the 'Victory' gesture, two NC2 transducers were attached to the index and middle fingers at joint positions as shown in Fig. 5(d) and the output voltage was measured to be ~6 V. For the 'Ok' gesture, two NC2 transducers were attached to the thumb and index finger and an output voltage of ~10 V was measured. Similarly, for the 'Stop' gesture, three NC2 transducers were attached to the index, middle and ring fingers, the output voltage was measured to be ~14 V, and the comparatively recorded output voltages are shown in Fig. 5(e). From the observation, the real-time voltage output corresponding to each gesture exhibited unique signal amplitudes, enabling reliable differentiation. The 'Stop' configuration generated the highest output voltage among the tested gestures because three NC2 films were connected in series, resulting in a higher voltage output for this gesture than for the other gestures. This behavior demonstrates the capability of the ME nanogenerator to translate subtle gesture motions into distinct electrical signatures. Such gesture-specific signal responses confirm the device's high sensitivity and rapid signal transduction, validating its applicability in

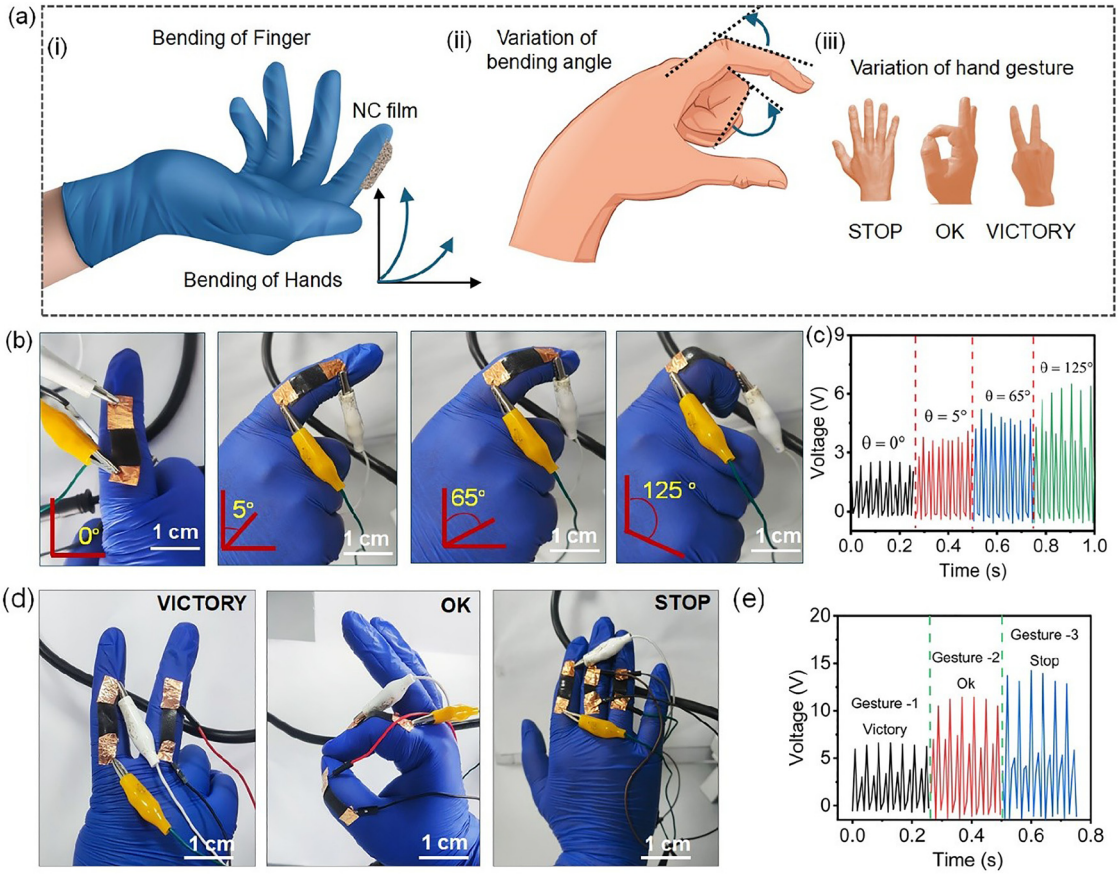


Fig. 5 (a) Illustration of real-time gesture-controlled HMI systems, distinct finger bending, and gestures. (b) Demonstration of index finger bending at 0°, 5°, 65°, and 125° using the NC2 film. (c) Output voltage of finger bending orientation from the NC2 film. (d) Demonstration of 'Victory', 'Ok', and 'Stop' gestures using the NC2 film. (e) Recorded output voltage of the gestures from the NC2 film.

next-generation stretchable electronics. The demonstrated approach offers a promising pathway toward the application of low-power, self-powered HMI systems in intelligent prosthetics, sign-language recognition, and personalized healthcare interfaces.

## 4. Conclusion

In summary, we have designed a highly stretchable and self-powered ME composite film by embedding $Ni_{0.5}Co_{0.5}Fe_2O_4$ nanoparticles into a soft Ecoflex matrix, aimed at wearable energy harvesting and real-time gesture-responsive human–machine interface applications. The ME films exhibited high mechanical stretchability, sustaining tensile strains up to ~315% without performance degradation. They retained over ~100% of their initial output after 1000 continuous stretching–release cycles, confirming their mechanical durability. The optimized device generated significant ME output voltages, maintained stability under repeated mechanical strain, and enabled efficient energy harvesting from ambient magnetic field sources. The ME device generated a peak output voltage of ~8.3 V and a maximum power density of ~3.16 mW $cm^{-3}$, outperforming conventional soft nanogenerators. The ME device demonstrated high performance in real-time experiments, where distinct output voltages were associated with specific finger bending and hand gestures. Integrating the fabricated flexible ME film into skin-interfaced platforms enables simultaneous powering, sensing, and energy harvesting without requiring an external power source. This work paves the way for the next generation of magnetoelectrically active, skin-conformal devices with applications in smart prosthetics, autonomous soft robotic interfaces, and gesture-based control systems.

## Conflicts of interest

All authors declare no competing financial interests.

## Data availability

All data is available from the corresponding author upon reasonable request. Supplementary information: Additional experimental details, preparation of the film, optical image of the device, experimental setup, characterization of the nanoparticles, durability test and output voltage under different hand gestures. See DOI: **https://doi.org/10.1039/d5tc03220b**.

## Acknowledgements

S. K. Y. thanks Christ University for providing financial support. P. K. acknowledges the funding support from Science and Engineering Research Board (currently ANRF), India, for the sponsored project (SRG/2023/001763).

## References

1 T. Q. Trung and N.-E. Lee, Recent Progress on Stretchable Electronic Devices with Intrinsically Stretchable Components, *Adv. Mater.*, 2017, **29**(3), 1603167, DOI: **10.1002/adma.201603167**.

2 M. T. Rahman, M. S. Rahman, H. Kumar, K. Kim and S. Kim, Metal-Organic Framework Reinforced Highly Stretchable and Durable Conductive Hydrogel-Based Triboelectric Nanogenerator for Biomotion Sensing and Wearable Human-Machine Interfaces, *Adv. Funct. Mater.*, 2023, **33**(48), 2303471, DOI: **10.1002/adfm.202303471**.

3 Y. Liu, S. D. Mulatier and N. Matsuhisa, Unperceivable Designs of Wearable Electronics, *Adv. Mater.*, 2025, 2502727, DOI: **10.1002/adma.202502727**.

4 Y. Zhang, Z. Xu, Y. Yuan, C. Liu, M. Zhang, L. Zhang and P. Wan, Flexible Antiswelling Photothermal-Therapy MXene Hydrogel-Based Epidermal Sensor for Intelligent Human–Machine Interfacing, *Adv. Funct. Mater.*, 2023, **33**(21), 2300299, DOI: **10.1002/adfm.202300299**.

5 R. D. Salian, S. Mishra, C. C. Gowda, R. K. Barik, A. K. Singh, C. S. Tiwary and P. Kumbhakar, Defect Engineered Few Layered $MoS_2$ for Human–Machine Interface, *Small methods*, 2025, 2500068, DOI: **10.1002/smtd.202500068**.

6 K. Kim, D. R. Kim, D. Kim, H. H. Song, S. Lee, Y. Choi, K. Lee, G. H. Lee, J. Lee, H. H. Kim, E. Ahn, J. H. Jang, Y. Kim, H. C. Lee, Y. Kim, S. I. Park, J. Yoo, Y. Lee, J. Park, D.-H. Kim, M. K. Choi and J. Yang, Intrinsically-Stretchable and Patternable Quantum Dot Color Conversion Layers for Stretchable Displays in Robotic Skin and Wearable Electronics, *Adv. Mater.*, 2025, 2420633, DOI: **10.1002/adma.202420633**.

7 Q. Shi, B. Dong, T. He, Z. Sun, J. Zhu, Z. Zhang and C. Lee, Progress in wearable electronics/photonics—Moving toward the era of artificial intelligence and internet of things, *InfoMat*, 2020, **2**(6), 1131–1162, DOI: **10.1002/inf2.12122**.

8 J. Xu, X. Li, H. Chang, B. Zhao, X. Tan, Y. Yang, H. Tian, S. Zhang and T.-L. Ren, Electrooculography and Tactile Perception Collaborative Interface for 3D Human–Machine Interaction, *ACS Nano*, 2022, **16**(4), 6687–6699, DOI: **10.1021/acsnano.2c01310**.

9 W. Wang, D. Yao, H. Wang, Q. Ding, Y. Luo, H. Ding, J. Yu, H. Zhang, K. Tao, S. Zhang, F. Huo and J. Wu, A Breathable, Stretchable, and Self-Calibrated Multimodal Electronic Skin Based on Hydrogel Microstructures for Wireless Wearables, *Adv. Funct. Mater.*, 2024, **34**(32), 2316339, DOI: **10.1002/adfm.202316339**.

10 S.-K. Lee, B. J. Kim, H. Jang, S. C. Yoon, C. Lee, B. H. Hong, J. A. Rogers, J. H. Cho and J.-H. Ahn, Stretchable Graphene Transistors with Printed Dielectrics and Gate Electrodes, *Nano Lett.*, 2011, **11**(11), 4642–4646, DOI: **10.1021/nl202134z**.

11 J.-H. Lee, K. Y. Lee, M. K. Gupta, T. Y. Kim, D.-Y. Lee, J. Oh, C. Ryu, W. J. Yoo, C.-Y. Kang, S.-J. Yoon, J.-B. Yoo and S.-W. Kim, Highly Stretchable Piezoelectric-Pyroelectric Hybrid Nanogenerator, *Adv. Mater.*, 2013, **26**(5), 765–769, DOI: **10.1002/adma.201303570**.

12 M. Salauddin, S. M. S. Rana, M. Sharifuzzaman, H. S. Song, M. S. Reza, S. H. Jeong and J. Y. Park, Highly Electronegative V2CTx/Silicone Nanocomposite- Based Serpentine Triboelectric Nanogenerator for Wearable Self-Powered Sensors and Sign Language Interpretation, *Adv. Energy Mater.*, 2023, **13**(10), 2203812, DOI: **10.1002/aenm.202203812**.

13 Z. Liu, H. Li, B. Shi, Y. Fan, Z. L. Wang and Z. Li, Wearable and Implantable Triboelectric Nanogenerators, *Adv. Funct. Mater.*, 2019, **29**(20), 1808820, DOI: **10.1002/adfm.201808820**.

14 P. Wojciak, J. G. Smith, T. Hallam and S. Seyedin, Piezoelectric Polyurethane/Barium Titanate Composites with High Stretchability and Voltage Output for Energy Harvesting in Soft Wearable Electronics, *Adv. Mater. Technol.*, 2025, 2500248, DOI: **10.1002/admt.202500248**.

15 S. K. Yadav and J. Hemalatha, Synthesis and characterization of magnetoelectric $Ba_2Zn_2Fe_{12}O_{22}$–$PbZr_{0.52}Ti_{0.48}O_3$ electrospun core–shell nanofibers for the AC/DC magnetic field sensor application, *Appl. Phys. A*, 2024, **130**, 67, DOI: **10.1007/s00339-023-07158-z**.

16 S. K. Yadav and J. Hemalatha, Direct magnetoelectric and magnetodielectric studies of electrospun $Ba_2Ni_2Fe_{12}O_{22}$–$Pb(Zr_{0.52}Ti_{0.48})O_3$ core–shell nanofibers, *J. Magn. Magn. Mater.*, 2022, **564**, 170174, DOI: **10.1016/j.jmmm.2022.170174**.

17 F. Narita and M. Fox, A Review on Piezoelectric, Magnetostrictive, and Magnetoelectric Materials and Device Technologies for Energy Harvesting Applications, *Adv. Energy Mater.*, 2018, **20**(5), 1700743, DOI: **10.1002/adem.201700743**.

18 M. Mariello and C. M. Proctor, Wireless Power and Data Transfer Technologies for Flexible Bionic and Bioelectronic Interfaces: Materials and Applications, *Adv. Mater. Technol.*, 2025, **10**(5), 2400797, DOI: **10.1002/admt.202400797**.

19 P. Costa, J. N.-Pereira, N. Pereira, N. Castro, S. Gonçalves and S. Lanceros-Mendez, Recent Progress on Piezoelectric, Pyroelectric, and Magnetoelectric Polymer-Based Energy-Harvesting Devices, *Energy Technol.*, 2019, 7(7), 1800852, DOI: **10.1002/ente.201800852**.

20 Z. Zhang, L. Wang, H. Yu, F. Zhang, L. Tang, Y. Feng and W. Feng, Highly Transparent, Self-Healable, and Adhesive Organogels for Bio- Inspired Intelligent Ionic Skins, *ACS Appl. Mater. Interfaces*, 2020, **12**(13), 15657–15666, DOI: **10.1021/acsami.9b22707**.

21 X. Zeng, Z. Wang, H. Zhang, W. Yang, L. Xiang, Z. Zhao, L.-M. Peng and Y. Hu, Tunable, Ultrasensitive, and Flexible Pressure Sensors Based on Wrinkled Microstructures for Electronic Skins, *ACS Appl. Mater. Interfaces*, 2019, **11**(23), 21218–21226, DOI: **10.1021/acsami.9b02518**.

22 W. Deng, T. Yang, L. Jin, C. Yan, H. Huang, X. Chu, Z. Wang, D. Xiong, G. Tian, Y. Gao, H. Zhang and W. Yang,

Cowpea-structured PVDF/ZnO nanofibers based flexible self-powered piezoelectric bending motion sensor towards remote control of gestures, *Nano Energy*, 2019, **55**, 516–525, DOI: 10.1016/j.nanoen.2018.10.049.

23 A. S. Dahiya, F. Morini, S. Boubenia, K. Nadaud and D. Alquier, G. P.-Vittrant, Organic/Inorganic Hybrid Stretchable Piezoelectric Nanogenerators for Self-Powered Wearable Electronics, *Adv. Mater. Technol.*, 2017, **3**(2), 1700249, DOI: 10.1002/admt.201700249.

24 Q. Shia, Z. Zhang, T. Chene and C. Lee, Minimalist and multi-functional human machine interface (HMI) using a flexible wearable triboelectric patch, *Nano Energy*, 2019, **62**, 355–366, DOI: 10.1016/j.nanoen.2019.05.033.

25 Y. Jie, H. Zhu, X. Cao, Y. Zhang, N. Wang, L. Zhang and Z. L. Wang, One-Piece Triboelectric Nano sensor for Self-Triggered Alarm System and Latent Fingerprint Detection, *ACS Nano*, 2016, **10**(11), 10366–10372, DOI: 10.1021/acsnano.6b06100.

26 J. Ma, J. Hu, Z. Li and C.-W. Nan, Recent Progress in Multiferroic Magnetoelectric Composites: from Bulk to Thin Films, *Adv. Mater.*, 2011, **23**(9), 1062–1087, DOI: 10.1002/adma.201003636.

27 X.-K. Wei, N. Domingo, Y. Sun, N. Balke, R. E. Dunin-Borkowski and J. Mayer, Progress on Emerging Ferroelectric Materials for Energy Harvesting, Storage and Conversion, *Adv. Energy Mater.*, 2022, **12**(24), 2201199, DOI: 10.1002/aenm.202201199.

28 H. M. Shashanka, S. Saha, K. Haritha, P. N. Anantharamaiah and C. V. Ramana, Aluminum and Zinc Co-substituted Cobalt Ferrite: Structural, Magnetic, and Magnetostrictive Properties, *J. Phys. Chem. C*, 2023, **27**(23), 11218–11230, DOI: 10.1021/acs.jpcc.3c01361.

29 S. M. S. Rana, Md. A. Zahed, M. T. Rahman, M. Salauddin, S. H. Lee, C. Park, P. Maharjan, T. Bhatta and K. Shrestha, Jae Yeong Park, Cobalt-Nanoporous Carbon Functionalized Nanocomposite-Based Triboelectric Nanogenerator for Contactless and Sustainable Self-Powered Sensor Systems, *Adv. Funct. Mater.*, 2021, **31**(52), 2105110, DOI: 10.1002/adfm.20210511.

30 J. Halder, P. De and A. Chandra, Synergistic contribution of redox additive electrolytes to significantly increase the performances of hybrid supercapacitors, *J. Energy Storage*, 2024, **104**, 114583, DOI: 10.1016/j.est.2024.114583.

31 K. Ghosh, A. Morgan, X. Garcia-Casas and S. Kar-Narayan, Tailoring of Self-Healable Polydimethylsiloxane Films for Mechanical Energy Harvesting, *ACS Appl. Energy Mater.*, 2024, **7**(19), 8185–8195, DOI: 10.1021/acsaem.4c01275.

32 P. Sowjanya, N. P. Kumar, A. Chelvane and M. V. Ramana Reddy, Synthesis and analysis of low field high magnetostrictive Ni-Co ferrite for magneto-electric energy harvesting applications, *Mater. Sci. Eng. B*, 2022, **279**, 115674, DOI: 10.1016/j.mseb.2022.115674.

33 C.-W. Nan, N. Cai, Z. Shi, J. Zhai, G. Liu and Y. Lin, Large magnetoelectric response in multiferroic polymer-based composites, *Phys. Rev. B: Condens. Matter Mater. Phys.*, 2005, **71**, 014102, DOI: 10.1103/PhysRevB.71.014102.

34 G. He, Y. Jian, T. Ma, J. Niu, Y. Bai, N. Jiang, H. Chang and S. Zhao, Strain engineering for magnetoelectric coupling in flexible composite devices, *Appl. Phys. Lett.*, 2025, **126**, 182901, DOI: 10.1063/5.0271826.

35 M. Satish, H. M. Shashanka, S. Saha, K. Haritha, D. Das, P. N. Anantharamaiah and C. V. Ramana, Effect of High-Anisotropic $Co^{2+}$ Substitution for $Ni^{2+}$ on the Structural, Magnetic, and Magnetostrictive Properties of NiFe2O4: Implications for Sensor Applications, *ACS Appl. Mater. Interfaces*, 2023, **15**, 15691–15706, DOI: 10.1021/acsami.2c23025.

36 T. Dippong, E. A. Levei, O. Cadar, I. G. Deac, L. Diamandescu and L. Barbu-Tudoran, Effect of nickel content on structural, morphological, and magnetic properties of $Ni_xCo_{1-x}Fe_2O_4$/$SiO_2$ nanocomposites, *J. Alloys Compd.*, 2019, **786**(25), 330–340, DOI: 10.1016/j.jallcom.2019.01.363.

37 D. Kwon, T.-I. Lee, J. Shim, S. Ryu, M. S. Kim, S. Kim, I. T.-Soo Kim and I. Park, Highly Sensitive, Flexible and Wearable Pressure Sensor Based on a Giant Piezocapacitive Effect of Three- Dimensional Microporous Elastomeric Dielectric Layer, *ACS Appl. Mater. Interfaces*, 2016, **8**(26), 16922–16931, DOI: 10.1021/acsami.6b04225.

38 H. Jiang, X. Zou, P. Li, Z. Lin, X. Liu and X. Weng, Flexible Capacitive Pressure Sensor Enhanced by Black Phosphorus-Au Nanocomposites/Ecoflex Sponge for Pressure and Proximity Detection, *IEEE Sens. J.*, 2024, **24**(11), 17543–17550, DOI: 10.1109/JSEN.2024.3391340.

39 R. Elhajjar, C.-T. Law and A. Pegoretti, Magnetostrictive polymer composites: Recent advances in materials, structures and properties, *Prog. Mater. Sci.*, 2018, **97**, 204–229, DOI: 10.1016/j.pmatsci.2018.02.005.

40 S. Dong, J. F. Li, D. Viehland, J. Cheng and L. E. Cross, A strong magnetoelectric voltage gain effect in magnetostrictive-piezoelectric composite. Available to Purchase, *Appl. Phys. Lett.*, 2004, **85**, 3534–3536, DOI: 10.1063/1.1786631.

41 L. Cestarollo, S. Smolenski and A. El-Ghazaly, Nanoparticle-Based Magnetorheological Elastomers with Enhanced Mechanical Deflection for Haptic Displays, *ACS Appl. Mater. Interfaces*, 2022, **14**(16), 19002–19011, DOI: 10.1021/acsami.2c05471.

42 N. Ram, P. D. Prasad, J. Kaarthik, G.-T. Hwang, K. Vaduganathan and A. Venkateswarlu, High Output, Biocompatible, Fully Flexible Fiber-Based Magneto-Mechano-Electric Generator for Standalone-Powered Electronics, *Adv. Sustainable Syst.*, 2025, **9**, 2400548, DOI: 10.1002/adsu.202400548.

43 M. Koç, Ç. E. D. Dönmez, L. Paralı, A. Sarı and S. Aktürk, Piezoelectric and magnetoelectric evaluations on PVDF/$CoFe_2O_4$ based flexible nanogenerators for energy harvesting applications, *J. Mater. Sci.: Mater. Electron.*, 2022, **33**, 8048, DOI: 10.1007/s10854-022-07956-w.

44 A. Sasmal, S. Sen, J. A. Chelvane and A. Arockiarajan, PVDF-based flexible magnetoelectric composites for capacitive energy storage, hybrid mechanical energy harvesting and self-powered magnetic field detection, *Polymer*, 2023, **281**, 126141, DOI: 10.1016/j.polymer.2023.126141.

45 A. A. Chlaihawi, S. Emamian, B. B. Narakathu, B. J. Bazuin and M. Z. Atashbar, Novel screen printed and flexible low frequency magneto-electric energy harvester, *IEEE Sensors*, 2016, 1–3, DOI: 10.1109/ICSENS.2016.7808947.

 